Sun *Geosci. Lett.* (2016) 3:21
DOI 10.1186/s40562-016-0052-5

Geoscience Letters

RESEARCH LETTER Open Access

The vortex moving toward Taiwan and the influence of the central mountain range

Wen-Yih Sun[1,2,3*]

Abstract

Surface friction is important to a vortex moving toward Taiwan but was ignored in several previous studies. The change of the potential vorticity comes from friction in the shallow-water equation, hence, it was applied to study the westbound vortex influenced by the central mountain range (CMR) blocking and surface friction, which is defined as friction coefficient multiplied by the square root of topographic elevation. Without surface friction, the movement of vortex is not affected by the CMR due to the conservation of potential vorticity. With small surface friction, the simulated vortex first deflects southward slightly, then rebounds gently north due to the effect of channel flow, as the previous studies. With moderate or large surface friction, when the vortex approaching Taiwan, it deforms and creates two wind maxima; one due to effect of channel flow and the other on the east of the vortex, because the slowdown vortex is pushed by the mean easterly flow behind. Meanwhile, the vortex and two wind maxima rotate cyclonically. Hence, the vortex can deflect north or south, or form a loop, that depends on the strength and location of the wind maxima. If the circulation of the vortex moves around the northern tip of Taiwan, it can induce a significant secondary vortex on the lee side. On the other hand, the secondary vortex, triggered by the flow passing over the CMR, is rather weak. This paper may provide the formation of asymmetric inner flow and the deflection of the vortex, which may be difficult to define in a more complicated atmospheric model.

Keywords: Vortex, Potential vorticity, Surface friction, Deflect, Taiwan, CMR, Cyclonic circulation

Background

The CMR has a significant impact on the movement of the front (Sun and Chern 2006) and typhoons near Taiwan (Wang 1980; Shieh et al. 1998, etc.). The vortex passed an isolated island, has been widely investigated using observations and numerical models (Brand and Blelloch 1974; Wang 1980; Chang 1982; Bender et al. 1987; Yeh and Elsberry 1993; Lin et al. 2005; Huang and Lin 2008; Huang et al. 2011; Tang and Chan 2013, etc.). When a tropical cyclone (TC) moves toward Taiwan, the circulation and path may be significantly perturbed by the CMR. Observations showed that westbound typhoons tend to deflect northwestward around the northern side of the CMR (Wang 1980; Chang 1982). Wang (1980) suggested that this might be due to the deflection of the mean steering flow upstream of the CMR. Yeh and Elsberry's model simulations (1993) showed that vortices approaching the southern portion of the barrier were deflected to the south in a region approximately between 250 and 400 km upstream. When getting closer and approaching the southern part of the barrier, they were deflected northward, while those approaching the northern end were only slightly influenced. They proposed that it was the terrain-induced imbalance of the inner core structure led to the northward turn. Winds to the west of the storm were weakened by the topography, in particular, for those approaching the southern part of the barrier, because the cyclonic circulation impinged to a wider area of the topography which slows down the northerly channel flow. Hence, significant southerly asymmetric flow in the inner core may drift the vortex northward prior to landfall.

Without moist physics or effect of surface friction, Lin et al. (2005) conducted idealized simulations with much higher resolution over a bell-shaped topography. They

*Correspondence: wysun@purdue.edu
[1] Department of Earth, Atmospheric, and Planetary Sciences, Purdue University, 550 Stadium Mall Drive, West Lafayette, IN 47907-2051, USA
Full list of author information is available at the end of the article

introduced six non-dimensional parameters for TC track deflection. Track deflection has also been investigated by Huang and Lin (2008) using a shallow-water model. Both Lin et al. (2005) and Huang and Lin (2008) indicated that the parameter (R/Ly; where R is the radius of vortex, and Ly is the barrier scale in y-direction) is important to track deflection. The vortex tends to be deflected leftward (facing downstream), as it approaching the barrier with smaller R/Ly. Recently, Huang et al. (2011) found that typhoons approaching the northern and central idealized bell-shaped island are deflected significantly southward, while those approaching the southern part are barely deflected or deflected to the north. They are different from Yeh and Elsberry (1993)'s experiments: "In general, the vortices approaching the northern island experienced northward defections, and the vortices approaching the southern island first experienced southward deflections and then moves toward the north". Huang et al. (2011) suggested that the inner core asymmetric flow leading to the track deflection. Initially, the northerly flow enhanced by the channeling effect is to deflect the storm southward, and then due to effect of terrain, the northerly flow to the west of the storm weakens, and the southerly flow deflect the storm northward when it approaches to the northern bell-shaped island (in their Fig. 8). They also noted that the inner core asymmetric ventilation flow of typhoon Haitang (2005) does not match the movement of the deflected typhoon perfectly, partly because the steering flow is not well defined and could not completely capture the terrain-induced deflection in simulation and in nature. Huang et al. (2011) successfully simulated the looping motion observed in Typhoon Krosa (2007) with a fine resolution, realistic topography, although their simulated vortex turned northward after looping, but the observed one moved northwestward. The previous studies focus on the channeling-induced low-level jet; Wu et al. (2015) proposed that the leading role of the northerly asymmetric flow in the mid-troposphere causing the southward deflection of the simulated TC tracks; overall, their deep-layer areal-mean asymmetric flow is consistent with the movement of storm, although some discrepancy still exists.

Surface friction is important to the flow over mountains (Peng and Thompson 2003; Sun and Hsu 2005; Sun and Chern 2006; Sun 2013; Sun and Sun 2015). Previously, it is also believed that surface friction is secondary; therefore, it is not included in Lin et al. (2005); Huang and Lin (2008), and other studies. Furthermore, the atmospheric model is quite complicated and difficult to sort out the effect of individual forcing or provide a clear physical explanation of the deflection of the vortex. Furthermore, the deflection of the vortex can be quite different among the different models. To focus on the effect of surface friction and blocking on the movement of a vortex approaching Taiwan, we use real topography instead of an idealized bell-shaped mountain.

Here, a high-resolution shallow-water model is applied to study the interactions among vortex, topography, and surface friction which is a function of friction coefficient and topographic elevation. On a free-slip surface, the simulated vortex in an inviscid fluid does not deflect when it passes Taiwan. With surface friction, a vortex approaching Taiwan, it can deflect north or south, or form a loop depending on the steering wind, surface friction, initial location, and the structure of the vortex. The effect of blocking becomes larger for slower-moving vortices, as the previous studies. With weak surface friction, when the vortex approaching but before landing, the northerly flow enhanced by channeling effect deflects the storm southward; after it landing and the cyclonic circulation reaching the CMR, the northerly flow to the west of the storm is weakened by surface friction, and the vortex rebounds northward by a strong southerly flow on the east, which is similar to the previous studies: "In general, the vortices approaching the northern island experienced northward defections, and the vortices approaching the southern island first experienced southward deflections and then moves toward the north" according to Yeh and Elsberry (1993 on p. 3203) and Fig. 12a of Wu et al. (2015), but different from drastic change shown in Fig. 5 of Lin et al. (2005).

With moderate or strong surface friction, a vortex deforms, as it approaching Taiwan. The vortex forms two excessive velocity maxima: one on the west associated with channel flow and the other on the east caused by the mean flow pressing on the slowdown vortex. The simulated vortex trajectory is influenced by the rotation of the vortex and two velocity maxima. The intensity of vortex decreases quickly after circulation hits the CMR. The vortex can induce the secondary circulations on the west of the CMR. The secondary vortices caused by the flow passing the CMR are weak, those triggered by the circulations moving around the northern tip of the Island can be significant. Since the model does not include the effect of latent heat, vertical wind shear, and other physics, the simulations may not be able to fully represent the observed typhoon or compare with the simulations from the atmospheric model.

In an irrotational fluid, vorticity can be generated by friction in a uniform flow passed a free-slip mountain (Schar and Smith 1993). Hence, the results obtained from the model with horizontal friction can be different from the inviscid fluid simulations. It is also noted that adding diffusion in fluid dynamics equations in the leapfrog and forward–backward schemes can create unwanted instability (Sun 2010).

Methods

Basic equations

The equations of shallow water are

$$\frac{du}{dt} - fv = -g\frac{\partial(h+h_s)}{\partial x} - ku \tag{1}$$

$$\frac{dv}{dt} + fu = -g\frac{\partial(h+h_s)}{\partial y} - kv \tag{2}$$

$$\frac{dh}{dt} = -h\left(\frac{\partial u}{\partial x} + \frac{\partial v}{\partial y}\right), \tag{3}$$

where u and v are x- and y-component velocities, respectively; f is the Coriolis parameter, h is the depth of fluid, and h_s is the terrain height, $h_f = h + h_s$ is the free surface height, surface friction $k \equiv \alpha\sqrt{h_s}$, and α is a friction coefficient.

The potential vorticity equation becomes

$$\frac{d\Pi}{dt} = \frac{d}{dt}\left(\frac{\zeta+f}{h}\right) = \frac{1}{(\zeta+f)}\left(\frac{\partial(ku)}{\partial y} - \frac{\partial(kv)}{\partial x}\right), \tag{4}$$

where $\varsigma = \frac{\partial v}{\partial x} - \frac{\partial u}{\partial y}$ is the relative vorticity, and $\Pi \equiv \frac{\zeta+f}{h}$ is the potential vorticity (PV). The change of PV comes from friction and is not influenced by vertical stretching. It is easier to evaluate the change of the PV due to the effect of surface friction and topographic blocking than the relative vorticity budget (Sun et al. 1991; Sun and Chern 1993; Huang and Lin 2008; Huang et al. 2011, etc.). The simulations show that the location of PV maximum (which is referred as vortex center, VC) coincides with that of relative vorticity maximum before landing but they may be one grid different after.

Numerical model

It is important that flow in this 1.5-layer shallow-water model is comparable to that in the atmospheric troposphere (with a depth ~10 km), which is topped by an undisturbed stratosphere (Matsuno 1966). The reduced gravity $g' = 4$ m s^{-2}; a lower layer with a depth $H = 100$ m; the horizontal length scale $R = 0.2R^*$, where R^* is the radius of the vortex in the real atmosphere, and the Coriolis parameter $f = 2\Omega\sin\phi$ or $f = f_{23}$ ($\phi = 23°$N) $= 5.7 \times 10^{-5}$ s^{-1}. The peak of mountain height in the model, $h_m = 10$ m at the grid (100, 85), corresponds to the mountain peak of $h_m^* = 3658$ m in Taiwan with a 4 km horizontal resolution. Table 1a, b shows the radius of vortex (R), fluid depth (H), the height of mountain peak (h_m), Rossby number (Ro), Froude number of the mountain $\left(Fr = \frac{U}{\sqrt{g'h_m}}\right)$ (Sun and Chern 1994; Sun and Sun 2015), Froude number far away from topography ($Fr_\infty = \frac{U}{\sqrt{g'H}}$), and L_R/R, where L_R is the radius of deformation. They are quite comparable to the corresponding parameters in the atmosphere indicated by superscript *, which indicates that the major atmospheric dynamics of typhoon and the effect of the CMR are well represented by the current model. We do not compare the Reynolds number. In the laboratory and direct numerical simulation (DNS), the Reynolds number is based on the molecular viscosity, which is a function of fluid property (MacCall et al. 2015). However, eddy viscosity in the atmospheric models is a function of the flow, fluid property, and resolutions. The length scale of the Reynolds number over the CMR is also difficult to define. The flux form of Eqs. (1)–(3) is:

$$\frac{\partial h}{\partial t} = -\frac{\partial \psi}{\partial x} - \frac{\partial \varphi}{\partial y} \tag{5}$$

$$\frac{\partial \psi}{\partial t} + \frac{\partial(u\psi)}{\partial x} + \frac{\partial(v\psi)}{\partial y} - f\phi = -gh\frac{\partial(h+h_s)}{\partial x} - k\psi \tag{6}$$

$$\frac{\partial \varphi}{\partial t} + \frac{\partial(u\varphi)}{\partial x} + \frac{\partial(v\varphi)}{\partial y} + f\psi = -gh\frac{\partial(h+h_s)}{\partial y} - k\varphi, \tag{7}$$

where $\psi = hu$ and $\varphi = hv$. Equations (5)–(7) are solved using Sun's scheme (2011), which is a fourth-order finite-volume scheme and requires very little or no smoothing (Sun 2010, 2011). This model has successfully simulated the highly nonlinear shock waves in dam-breaking, and Boyd's (Boyd 1980, 1985) analytical solutions of nonlinear Rossby wave and embedded fine-scale circulation inside (Sun and Sun 2013), etc. The domain consists of 401 × 301 grids with $\Delta x = \Delta y = 800$ m, corresponding to the horizontal resolution of 4 km in the real world. The time interval Δt is 16 s. Initially, a vortex is added to a constant easterly flow U. When the initial vortex is given by the geostrophic wind, the surface height depression of the vortex is

$$\begin{aligned} h\prime &= -h_0' \Bigg/ \left(1 + \left(\frac{x-x_0}{R}\right)^2 + \left(\frac{y-y_0}{R}\right)^2\right) \\ &= -h_0' \Bigg/ \left(1 + \left(\frac{x-i_0\Delta x}{R}\right)^2 + \left(\frac{y-j_0\Delta y}{R}\right)^2\right), \end{aligned} \tag{8}$$

where h_0' is the initial amplitude. The center of the initial vortex is located at (x_0, y_0), i.e., at grid (i_0, j_0), with a horizontal length scale R. A gradient wind equation is also used as an initial condition for the vortex, in which the initial tangential velocity of the vortex is

Table 1 Parameters in atmosphere and in shallow-water model with (a) $R = 24$ km and $U = 0.8$ ms^{-1}, and (b) $R = 40$ km and $U = 1.2$ ms^{-1}

	R (km)	H (m)	f (10^{-5}s^{-1})	h_m(m)	Vel (m/s)	N or. g'	R_0	L_R	Fr_m	Fr_α
(a)										
Atm	$R^* = 120$	$H^* = 10^4$	5.783	$h_m{}^* = 3500$	$U^* = 0\ 4$	$N = 10^{-2}$ s^{-1}	$U^*/f^*R^* = 0.58$	$NH^*/(f^*R^*) = 10^2/(f^*R^*) = 14.41$	$U^*/(Nh_m) = U/(35\ \text{ms}^{-1}) = 0.11$	$U^*/(NH^*) = 0.04$
Water	$R = 24$	$H = 100$	5.783	$h_m = 10$	$U = 0.8$	$g' = 4$ m s^{-2}	$U/fR = 0.58$	$\sqrt{g'H}/(fR) = 20/(fR) = 14.41$	$U/\sqrt{g'h_m} = 0.2U^*/6.3$ $= U/(32\ \text{ms}^{-1}) = 0.12$	$U/\sqrt{g'H} = 0.04$
(b)										
Atm	$R^* = 200$	10^4	5.783	3500	$U^* = 0\ 6$	$N = 10^{-2}$ s^{-1}	$U^*/f^*R^* = 0.52$	$NH^*/(f^*R^*) = 8.65$	$U^*/(Nh_m) = 0.17$	$U^*/(NH^*) = 0.06$
Water	$R = 40$	$H^* = 100$	5.783	10	$U = 1.2$	$g' = 4$ m s^{-2}	$U/fR = 0.53$	$\sqrt{g'H}/(fR) = 8.65$	$U/\sqrt{g'h_m} = 0.19$	$U/\sqrt{g'H} = 0.06$

$$V_0 = V_{\max}\frac{r}{r_{\max}}\exp\left\{\frac{1}{2}\left[1-\left(\frac{r}{r_{\max}}\right)^2\right]\right\}, \quad (9)$$

where $V_{\max}$ is the maximum tangential velocity at radius $r_{\max}$ (Chang 1982; Lin et al. 2005).

Results and discussions

Numerical simulations without vortex

Without surface friction (i.e., $\alpha = 0$) or horizontal friction/smoothing, the streamlines of perturbation velocity field $[u'\ (=u - U), v]$ departing from the mean wind, $U = -1.2$ m s^{-1} ($U^* = -6$ m s^{-1} in the atmosphere) at $t = 86{,}400$ s, are shown in Fig. 1a, in which contours of elevation are $h_m = 1$, 2, 3, 4, and 5 m ($h_m^* = 360$, 720, 1080, 1440, and 1800 m), the elevation higher than 5 m (1800 m in real world) in the CMR is blanked in all figures. The perturbation wind speed $u' \leq 0.093$ m s^{-1} is much less than the mean wind of -1.2 m s^{-1}. The block of the CMR and the NNE–SSW orientation of the Island introduce a weak anticyclonic circulation, similar to a high pressure on the inward side of an isolated island in the atmosphere model with the earth rotation (Sun et al. 1991; Sun and Chern 1993, 1994, 2006). Because of small

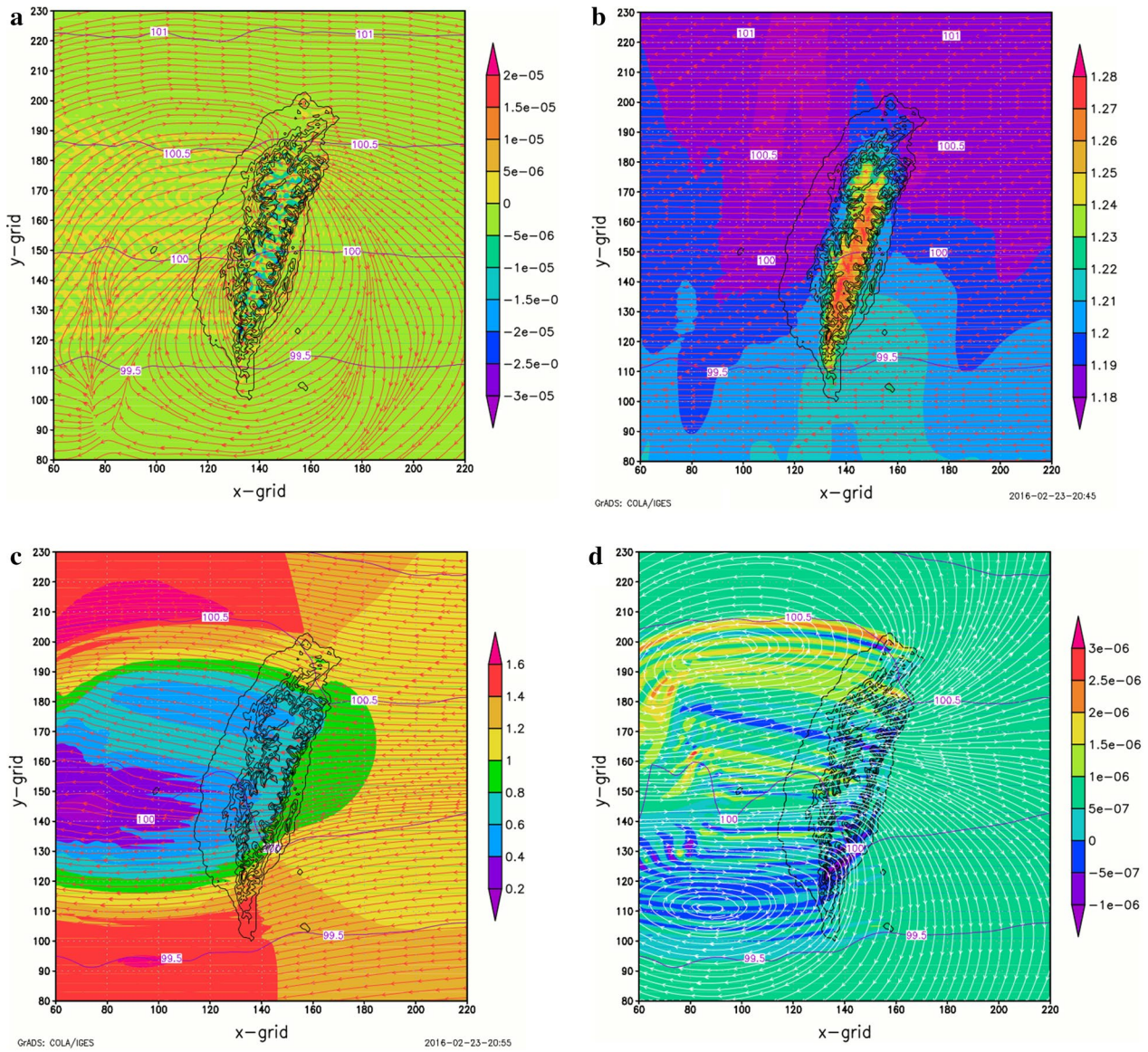

Fig. 1 **a** Streamline of $(u - U, v)$ and ς (*shaded color*). **b** Streamline of (u, v) and $|V|$ (*shaded color*) with $\alpha = 0$. **c** Same as **b** except $\alpha = 5 \times 10^{-5}$ m$^{-1/2}$ s^{-1}. **d** Streamline of $(u - U, v)$ and PV (*shaded color*) with $\alpha = 5 \times 10^{-5}$ m$^{-1/2}$ s^{-1} at $t = 86{,}400$ s. *black lines* are between coast and $h_s = 5$ m, and it is blank for $h_s > 5$ m

h_m/H, small patches of slightly negative relative vorticities (shaded color) form over the rugged mountains. The streamlines of total velocity (Fig. 1b) reveal that wind speed (shaded color) increases but direction does not change over the CMR. Combining the increase of wind speed and the decrease of depth results in a less change of the mass flux (h**V**) over the CMR. The movement of flow depends on the mass flux instead of velocity. Hence, the impact of the mountains is not significant in this inviscid case.

With surface friction, $\alpha = 5 \times 10^{-5}$ m$^{-1/2}$ s^{-1}, and $U = -1.2$ m s^{-1} ($U^* = -6$ m s^{-1}), the streamlines and speed (shaded color) at $t = 86{,}400$ s (24 h) in Fig. 1c show that wind slows down when it approaches the island, and the speed further decreases over the mountains and the wake. Strong wind also develops to the northern and southern ends of Taiwan and beyond. The wind bends northward when it comes from northeast; it defects southward if it comes from southeast, which is similar to Fig. 9 of Yeh and Elsberry (1993). Figure 1d shows a positive PV in the northwestern Taiwan and the downstream region, and a negative PV in the southern Taiwan and the downstream area. They gradually propagate downstream with the mean wind, as discussed in Sun and Chern (1993, 1994).

Initial vortex from gradient wind equation

Initially, we set friction coefficient $\alpha = 1.0^{-4}$ m$^{-1/2}$ s^{-1}, $f = f_{23} = 5.7 \times 10^{-5}$ s^{-1}, $U = -0.8$ m s^{-1}, $V_{max} = 5.2$ m s^{-1}, and $r_{max} = 32$ km ($U^* = 4$ m s^{-1}, $V^*_{max} = 21$ m s^{-1}, and $r^*_{max} = 150$ km) in Eq. (9); the VC is located at grid (268, 170) initially. Figure 2 shows the trajectory of the PV with contour $= 6.8 \times 10^{-6}$ m^{-1} s^{-1} from $t = 0$ to $t = 2.688 \times 10^5$ s (=74.67 h). The vortex moves westward before $t = 115{,}200$ s (=32 h), after that, it changes to northwest direction, then moves around Taiwan, and stops near the southeastern coast (Tai-Dong) after $t = 2.688 \times 10^5$ s ~3.11 days. The trajectory is quite complicated even at early stage due to an irregular shape of the vortex. The vortex moving around Taiwan also occurs in Fig. 4i, j, k, and l of Huang and Lin (2008). Without mean flow, a perfect circular flow can preserve according to the gradient wind equation, but it fails with a mean flow. According to geostrophic adjustment (Sun

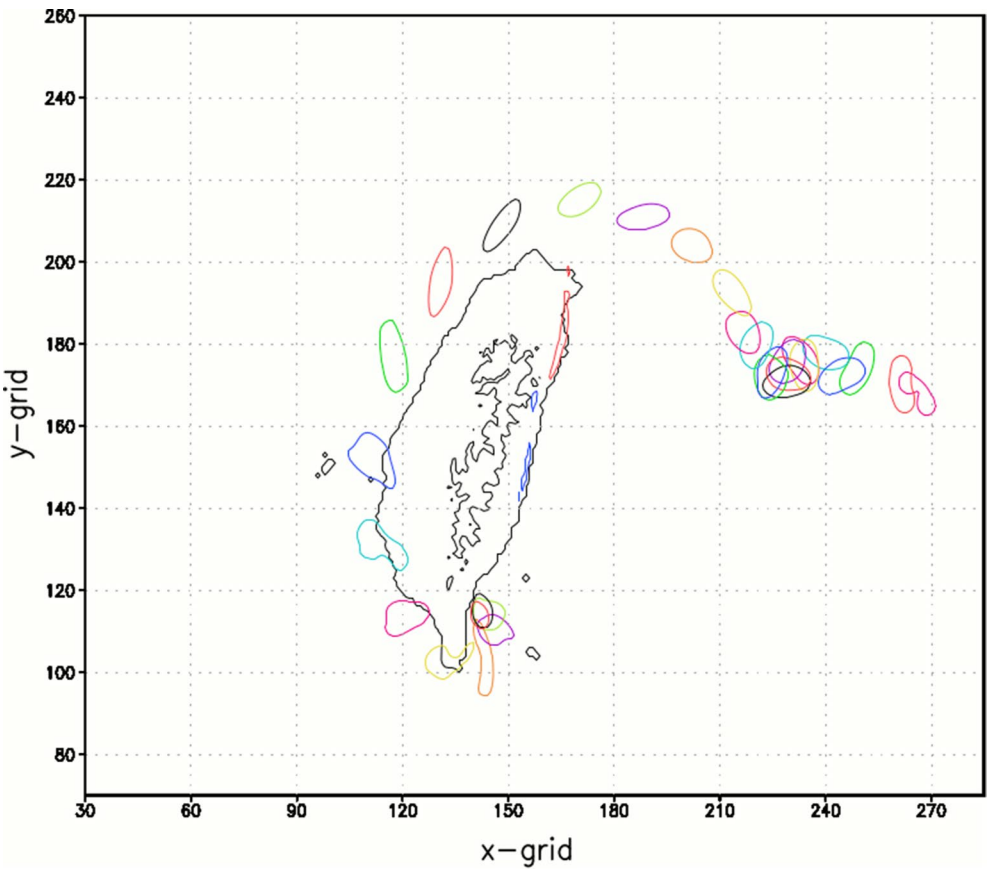

Fig. 2 Trajectory of PV from $t = 0$–3.1 days (contour is 6.8×10^{-6} m^{-1} s^{-1}). The initial wind of vortex is given by gradient wind

2007), since the size of vortex is much smaller than the radius of deformation (i.e., $L_R \gg 1$ in Table 1a, b), the mass field (water depth) adjusts to the velocity field given by Eq. (9). Because the gradient wind already includes the centripetal force without mean flow, the mass field has little room to change compared with the vortex assumed in geostrophic wind balance initially. Hence, the initial condition of the imbedded vortex is given by the geostrophic wind in this study. More geostrophic adjustment will be presented in "Group A: inviscid cases with $\alpha = 0$ and $U = -1.2$ m s^{-1} ($U^* = -6$ m s^{-1})" section.

Vortices with geostrophic balance initially

Group A: inviscid cases with $\alpha = 0$ and $U = -1.2$ m s^{-1} ($U^* = -6$ m s^{-1})

Figure 3a shows the trajectories of vorticities A_1, A_2, and A_3, initially located at grids (280, 170), (280, 150), and (280,130), which are referred to as LN (location north), LC (location center), and LS (location south), respectively. The amplitudes of the initial surface depression (h_0') are 2, 3, and 4 m; the initial radii R are 16, 24, and 40 km ($R^* = 80$, 120, and 200 km). The trajectories incline slightly southward by the anticyclonic circulation, as discussed in Fig. 1a, b. The movement of vortices is independent of size or intensity (Fig. 3a). The streamlines, y-component flux hv (in green), and wind speed (in red) at 96,000 s (26.7 h) for A_2 in Fig. 3b reveal that the radius of the maximum y-component wind, $r_{mv} = 12$ km, and y-component maximum velocity, $v_m = 5.4$ m s^{-1} ($r_{mv}^* = 60$ km, and $v_m^* = 27$ m s^{-1}). The y-component fluxes are still quite symmetric to the VC when it is located over the CMR (Fig. 3b).

$\frac{d}{dt}\left(\frac{\zeta+f}{h}\right) = \frac{\partial}{\partial t}\left(\frac{\zeta+f}{h}\right) + V \cdot \nabla\left(\frac{\zeta+f}{h}\right) = 0$ in an inviscid flow. The budget of PV (Fig. 3c–e) shows the local rate of change, advection, and their summation at $t = 96{,}000$ s. Except a few spikes over the mountains due to nonlinear interaction between the flow and the topography which consists of many short waves, the total derivative = 0 proves that the PV is conserved when the vortex passes the mountains.

Figure 4a–c presents h_f (m), y-component velocity v (m s^{-1}), and PV (m^{-1} s^{-1}) along the west–east line passing through grid $j_0 = 150$ at $t = 0$, 9600, 19,200, 28,800, 38,400, and 48,000 s for A_2. At the beginning, the water near the vortex center is pushed away by centripetal force and drops quickly; meanwhile, the pressure gradient increases (Fig. 4a) to counterpoise the centripetal and Coriolis forces. The fluctuation of h_f after t = 9600 s comes from the rotation of vortex with asymmetric velocity and water depth. After $t = 9600$ s, the maximum y-component velocity $v_m \cong 5.3$ m s^{-1} at $r_m = 15$ km ($v_m^* = 26.5$ m s^{-1} at $r_{mv}^* = 75$ km), which is close to $v_m \cong 5.7$ m s^{-1} at $r_m = 12$ km ($v_m^* = 28.5$ m s^{-1} at $r_{mv}^* = 60$ km) initially (Fig. 4b). Because the size of vortex is much less than the radius of deformation, the height field changes drastically to adjust to the velocity field, as discussed in Sun (2007).

Trajectories of PV with surface friction

The trajectories of the vortex with $h_0' = 2$ m and $R = 16$ km ($R^* = 80$ km) are shown in Fig. 5a, in which the solid lines represent the trajectories with $U = -1.2$ m s^{-1} ($U^* = -6$ m s^{-1}); dashed–doted lines with $U = -0.8$ m s^{-1} ($U^* = -4$ m s^{-1}); the line with * for $U = -1.0$ m s^{-1} ($U^* = -5$ m s^{-1}); the line with Δ for $U = -1.6$ m s^{-1} ($U^* = -8$ m s^{-1}), except the black solid line for F1 [with $U = -1.6$ m s^{-1} ($U^* = -8$ m s^{-1}), $\alpha = 1.5 \times 1.0^{-4}$ m$^{-1/2}$ s^{-1}, starting at LN]; and the lines with o including the beta ($\beta = df/dy$) effect for B_1, B_2, and B_3 in Fig. 5a, and B_4 and B_5 in Fig. 5b; the yellow line with black dots for $\alpha = 0$ (no friction) for A_1, A_2, A_3, and B_4; magenta for $\alpha = 1 \times 10^{-5}$ m$^{-1/2}$ s^{-1}; cyan for $\alpha = 3 \times 10^{-5}$ m$^{-1/2}$ s^{-1}; green for $\alpha = 5 \times 10^{-5}$ m$^{-1/2}$ s^{-1}; blue for $\alpha = 8 \times 10^{-5}$ m$^{-1/2}$ s^{-1}; red for $\alpha = 1 \times 10^{-4}$ m$^{-1/2}$ s^{-1}; and black for $\alpha = 1.5 \times 1.0^{-4}$ m$^{-1/2}$ s^{-1}. The trajectories of vortices with $h_0' = 3$ m and $R = 24$ km ($R^* = 120$ km) are shown in Fig. 5b; with $h_0' = 4$ m and $R = 40$ km ($R^* = 200$ km) in Fig. 5c, which also include red o for the trajectory of D3 starting at LC with $\alpha = 10^{-4}$ s^{-1} m^{-1}, $h_0' = 5$ m, $R = 40$ km, and $U = -1.2$ m s^{-1} ($R^* = 200$ km and $U^* = -6$ m s^{-1}). The experiments are listed in Table 2a–c.

Since there is no surface friction over the ocean, at beginning, vortices move westward with slightly southward tilt, as discussed in the inviscid cases of Group A. The vortices with beta effect ($\beta = df/dy$) deflect slightly northward initially, because higher value of f is carried southward by cyclonic circulation ahead of the vortex. When approaching the Island, they behave similar to those without β but with a smaller southward deflection because of different impinging angles, except the inviscid B_4. Tang and Chan (2013) also included the beta-effect but no prevailing wind. For moderate surface friction (3×10^{-5} s^{-1} m$^{-1/2}$ $\leq \alpha \leq$ 8×10^{-5} s^{-1} m$^{-1/2}$), when the vortices move closer to the Island, they curve southward significantly, then most of them rebound north drastically before landing. For large surface friction, vortices may move southward without northward rebound, except those from LN. Based on surface friction, the results are divided into four groups:

Group C: vortices with 3×10^{-5} s^{-1} m$^{-1/2}$ $\leq \alpha \leq 8 \times 10^{-4}$ s^{-1} m$^{-1/2}$

This group includes Case C_1 with $\alpha = 5 \times 10^{-5}$ m$^{-1/2}$ s^{-1}, $h_0' = 3$ m, $R = 24$ km, $U = -1.2$ m s^{-1} ($R^* = 120$ km and

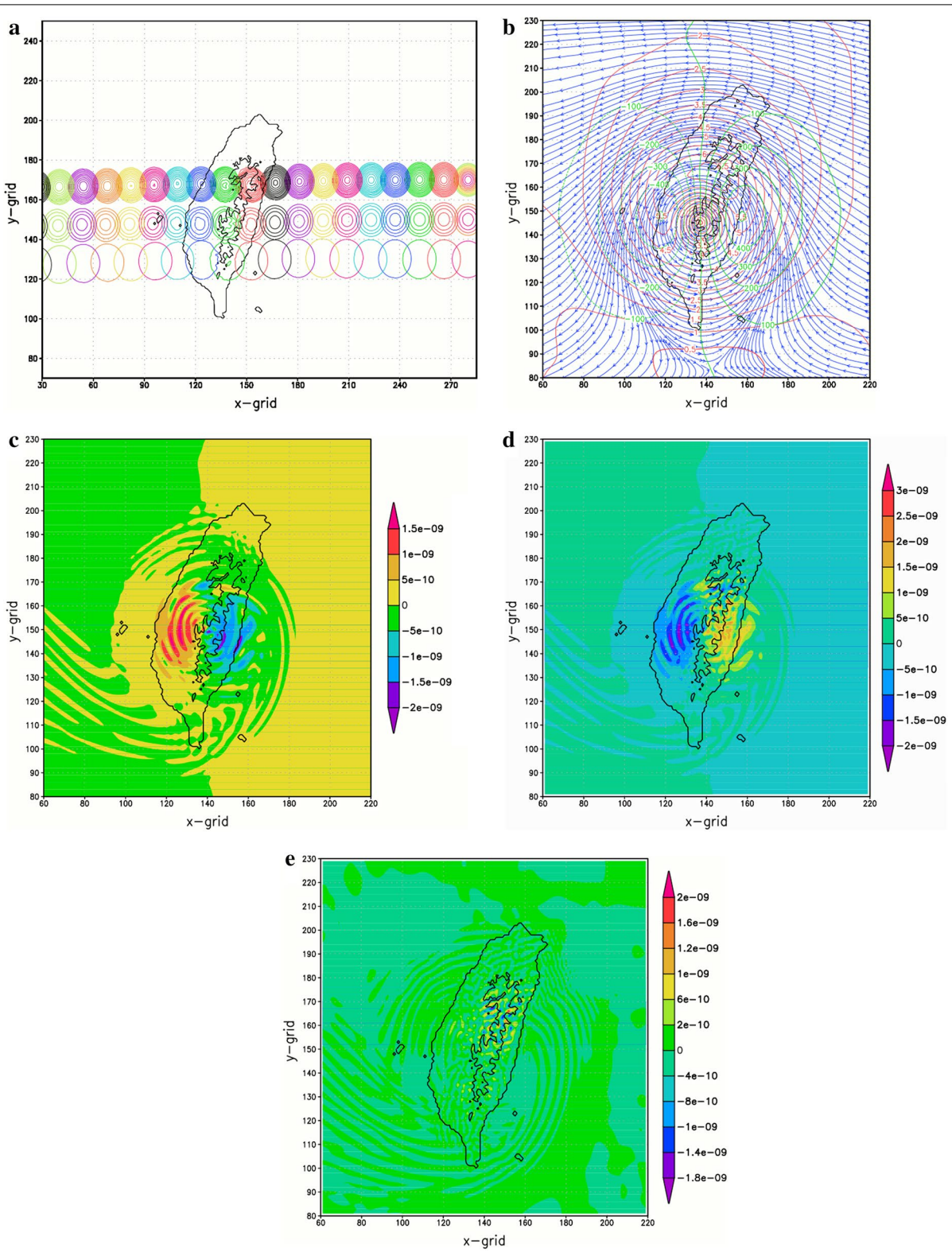

Fig. 3 **a** Trajectories for A_1 (contours from 1.2×10^{-5} to 2.2×10^{-5} m^{-1} s^{-1}), A_2 (contours from 1.2×10^{-5} to 1.5×10^{-5} m^{-1} s^{-1}), and A_3 (contour is 6×10^{-6} m^{-1} s^{-1}) with $\alpha = 0$; *black line* is $h_s = 5$ m; **b** Streamline, wind *V* (*red*) and *y*-component mass flux, *hv* (*green*); PV budget for: **c** local rate of change, **d** advection, and **e** total derivative for A_2 at $t = 96{,}000$ s

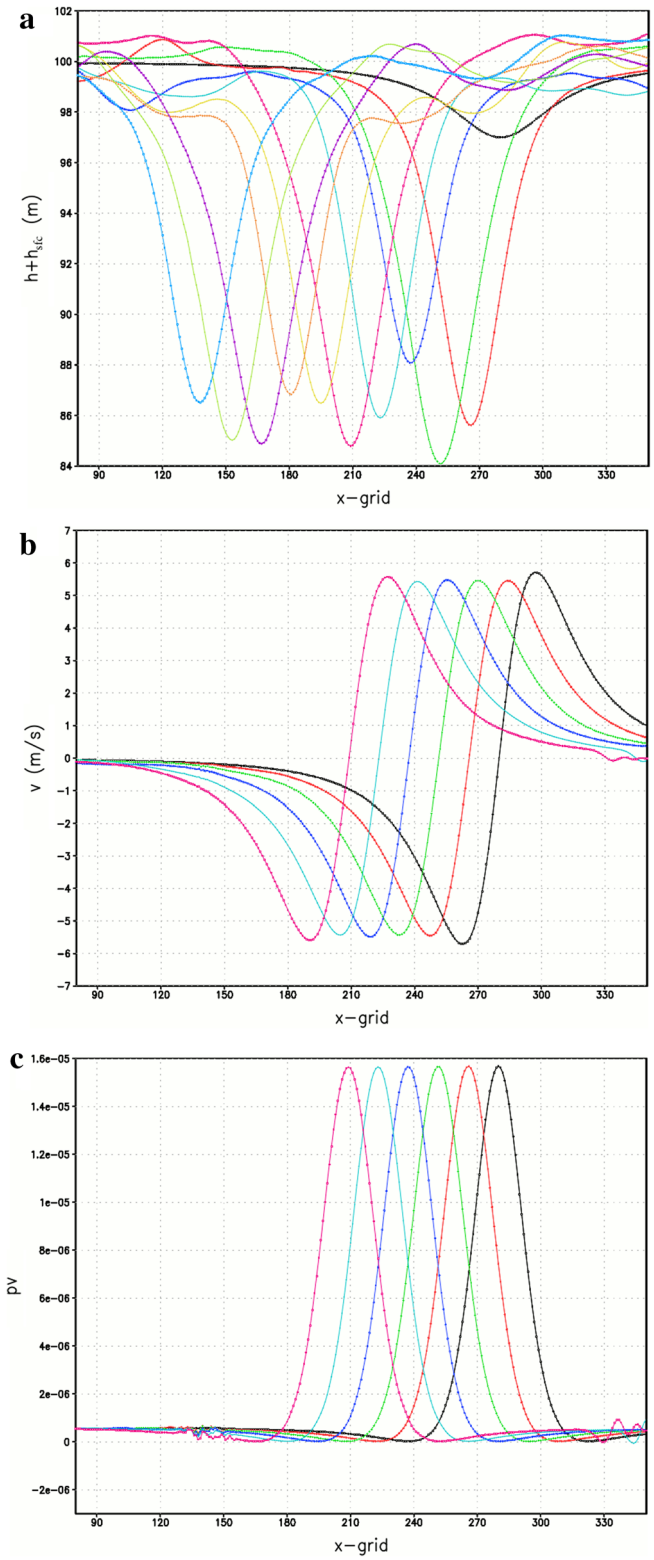

Fig. 4 **a** Surface height h_f (m) along $j_0 = 150$ for A_2 at $t = 0$ (*black*), 9600 (*red*), 19,200 (*green*), 28,800 (*dark blue*), 38,400 (*light blue*), and 48,000 s (*magenta*), **b** for v (m s^{-1}), and **c** for PV (m^{-1} s^{-1})

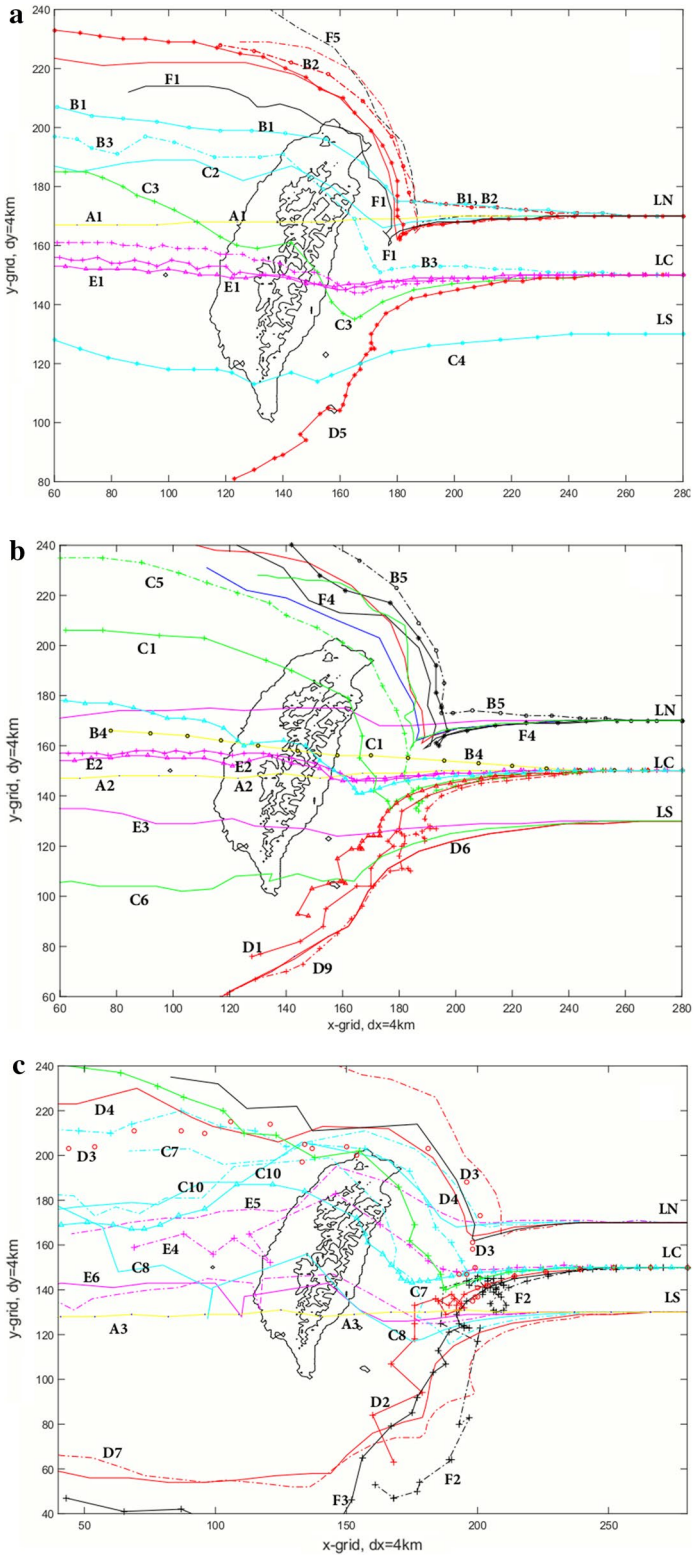

Fig. 5 Trajectories of PV with: **a** $h_0' = 2$ m, $R = 16$ km; **b** $h_0' = 3$ m, $R = 24$ km, and **c** $h_0' = 4$ m, $R = 40$ km, except red o for D3 with $h_0' = 5$ m

Table 2 List of cases with (a) $h_0 = 2$ m in Fig. 5a, (b) $h_0 = 3$ m in Fig. 5b, and (c) $h_0 = 4$ and 5 m in Fig. 5c

Case	h_0 (m)	U^* (m/s)	R^* (km)	Location	α ($\times 10^{-5}$)	$\beta = df/dy$
(a)						
A_1	2	6	80	N	0	N
E_1	2	8	80	C	1	N
B_1	2	4	80	N	3	Y
B_3	2	4	80	C	3	Y
C_2	2	6	80	N	3	N
C_4	2	5.5	80	L	3	N
C_3	2	6	80	C	5	N
B_2	2	4	80	N	10	Y
D_5	2	5.5	80	C	10	N
F_1	2	8	80	N	15	N
F_5	2	4	80	N	15	N
(b)						
A_2	3	6	120	C	0	N
B_4	3	6	120	C	0	Y
E_2	3	8	120	C	1	N
E_3	3	6	120	L	1	N
C_6	3	6	120	L	5	N
C_5	3	4	120	C	5	N
C_1	3	6	120	C	5	N
C_8	3	6	120	N	8	N
D_1	3	6	120	C	10	N
D_9	3	4	120	C	10	N
D_6	3	6	120	L	10	N
B_5	3	4	120	N	15	Y
F_4	3	6	120	N	15	N
(c)						
A_3	4	6	200	L	0	N
E_5	4	4	200	N	1	N
E_4	4	4	200	C	1	N
E_6	4	4	200	L	1	N
C_8	4	6	200	L	3	N
C_7	4	4	200	L	3	N
C_{10}	4	6	200	N	3	N
C_9	4	6	200	C	5	C
D_4	4	6	200	N	10	N
D_2	4	6	200	C	10	N
D_7	4	4	200	L	10	N
D_3	5	6	200	C	10	N
F_3	4	6	200	C	10	N
F_2	4	4	200	C	15	N
F_3	4	4	200	C	15	N

$U^* = -6$ m s^{-1}), and initially located at LC, shown by the green line with plus(+) in Fig. 5b. The simulations of C1 in Fig. 6a–d show the streamlines, mass flux hV (white), surface depression h' (purple dashed lines), PV (shaded color), and the relative velocity with respect to VC, $V' = |\mathbf{V}'| = |\mathbf{V} - \mathbf{V}_{VC}|$ (in red, where $\mathbf{V}_{VC}$ is the velocity at vortex center) at $t = 57{,}600$ s (Fig. 6a), 86,400 s (Fig. 6b), 96,000 s (Fig. 6c), and 105,600 s (Fig. 6d), respectively. At $t = 57{,}600$ s (16 h) (Fig. 6a), the vortex is close to Taiwan, and terrain slows down the westward movement of the vortex. Over the CMR, the flux hV < 50 m^2 s^{-1} and $V < 0.5$ m s^{-1} ($V^* < -2.5$ m s^{-1}); but hV ~ 200 m^2 s^{-1} and $V \sim 2$ m s^{-1} ($V^* \sim 10$ m s^{-1}) off the eastern coast. Hence, a dark blue, purple strip of negative PV forms along the Eastern Coastal Mountain Range and the eastern slope of the CMR because of strong shear.

The vortex is also squeezed by the flow from behind. Hence, the vortex gradually deforms to oval shape with the excessive relative velocity maxima, $V'_m \sim 5.5$ m s^{-1} ($V^{*\prime}_m \sim 27.5$ m s^{-1}) (red line) on both the west and east of the vortex, corresponding to a strong northerly wind, $hv_m = -528$ m^2 s^{-1} and $v_m \sim -5.7$ m s^{-1} ($v^*_m \sim -28.5$ m s^{-1}), and a southerly wind, $hv_m = 508$ m^2 s^{-1} and 5. 5 m s^{-1} ($v^*_m \sim 27.5$ m s^{-1}). The velocity of the vortex, $\mathbf{V}_{CV} = (-1.10, -0.11)$ m s^{-1} ($\mathbf{V}^*_{CV} = (-5.5, -0.55)$ m s^{-1}), at $t = 57{,}600$ s. Within the inner core (i.e., PV > 0), the streamlines move from low h' (purple dashed line) to high h' on the west, but from high h' toward low h' on the east of the vortex. The flux also carries high PV to west–southwest (WSW) and low PV to the east–northeast (ENE) of the vortex in Fig. 6a.

The VC moves southwestward from grid (212, 148) to grid (177, 135) between 57,600 and 86,400 s. Meanwhile, the vortex and surrounding strips of negative PV rotate 90° cyclonically (Fig. 6b). The eccentricity of PV is larger than that of the velocity field. Therefore, high PV on the east (west) of the vortex goes north (south). At $t = 96{,}000$ s, the major axis of the vortex aligns NNE–SSW (Fig. 6c) with the maximum southerly wind $v_m = 6.2$ m s^{-1} ($v^* = 31$ m s^{-1}) on the east and northerly wind $v_m = -5.02$ m s^{-1} ($v^* = -25.1$ m s^{-1}) west of the vortex. On the NW of the vortex, part of streamlines intrudes into Hawlien-Taidong Valley along the Eastern Coast, which hampers the northerly flow west of the vortex. The vortex moves north–northwest with $\mathbf{V}_{CV} = (-0.214, 0.590)$ m s^{-1} ($\mathbf{V}^*_{CV} = (-1.07, -2.95)$ m s^{-1}).

Combining the flows from the ocean and exited from land forms a strong northwesterly flow, Vh ≥ 525 m^2 s^{-1} and $V \geq 5.5$ m s^{-1} ($V^* = -27.5$ m s^{-1}), to SSW of the vortex at $t = 105{,}600$ s (Fig. 6d), which is stronger than the northerly wind of $v = -5.02$ m s^{-1} ($v^* = -25.1$ m s^{-1}), as shown in Fig. 6c. Meanwhile, the radius of curvature of the flow with positive PV (green area) coming from the land decreases (i.e., relative vorticity increases due to stretching). Therefore, the size of the vortex decreases. Since the northwesterly flow is still weaker than the southeasterly flow [with Vh ≥ 600 m^2 s^{-1} and $V \geq 6.5$ m s^{-1} ($V^* = 32.5$ m s^{-1})] of the vortex, the VC moves from (176, 138) west–northwest to (171, 140) between 96,000 and 105,600 s. Asymmetry of vortex increases with time. The vortex continues to rotate and moves west–northwest; meanwhile, it induces a weak, secondary cyclonic circulation at 124,800 s near the southwestern coast, triggered by the flow passing over the CMR (Fig. 6e). The vortex lands around $t = 139{,}000$ s (not shown). The movement of typhoon affected by the cyclonic rotation of asymmetric flow in the inner core has been proposed by Jian and Wu (2008), Huang and

Lin (2008), and Wu et al. (2015). However, some discrepancy exists between their vortex movement and inner core asymmetric flow as discussed previously. The rotation of the vortex and two high-wind zones proposed here may provide an alternative mechanism for the formation of asymmetric flow in the inner core.

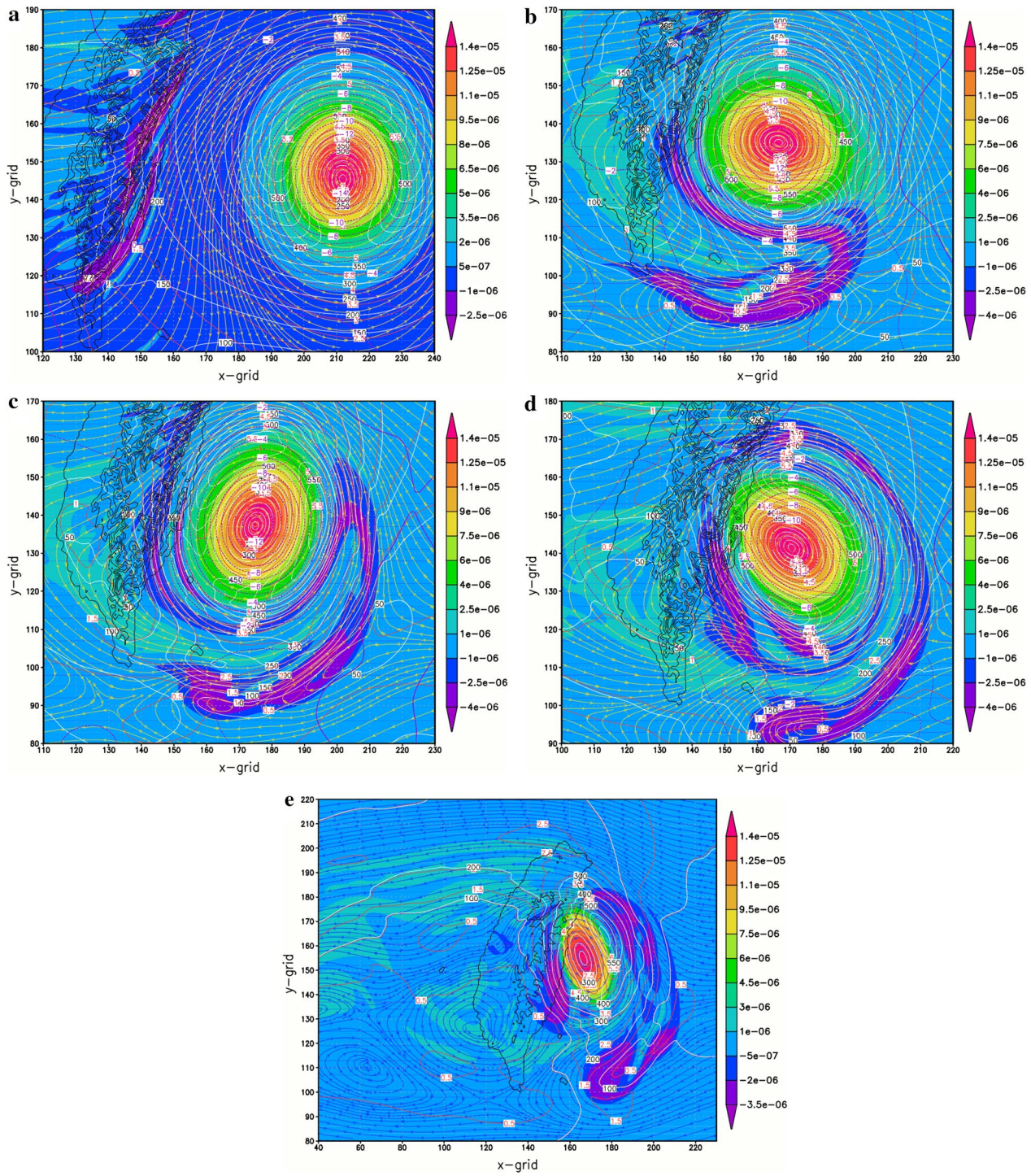

Fig. 6 PV (*shaded colors*), streamline, mass flux hV (*white*), and surface depression *h′* (*dashed purple*), and *V′* (*red*) for C_1 at: **a** $t = 48{,}000$ s, **b** $t = 86{,}400$ s, **c** $t = 96{,}000$ s, **d** $t = 105{,}600$ s, and **e** $t = 124{,}800$ s

Group D: vorticities with $a = 1 \times 10^{-4}\ m^{-1/2}\ s^{-1}$

Because of stronger surface friction, D1 [red line with + in Fig. 5b with $h_0' = 3$ m, $R = 24$ km, $U = -1.2$ m s^{-1} ($R_a = 120$ km and $U^* = -6.0$ m s^{-1}), at LC] moves westward slower than C_1. Figure 7a shows the vortex and the strips of negative PV (blue and purple) rotating cyclonically at $t = 86{,}400$ s, which is similar to C_1 in Fig. 6b. However, D_1 creates a stronger channel flow because of a wider gap and less flow moving over land. Since the northwesterly flux (~−575 m^2 s^{-1}) at the southwest of the vortex is stronger than the southeasterly flux (~525 m^2 s^{-1}) at northeast, the VC moves southeastward with $\mathbf{V}_{CV} = (0.325, -0.373)$ m s^{-1} ($\mathbf{V}^*_{CV} = (1.63, -1.87)$ m s^{-1}). The flow pattern at $t = 105{,}600$ s (Fig. 7b) shows the high wind and the front of negative PV strips originally south of vortex at $t = 86{,}400$ s (Fig. 7a) move to NNE of the vortex. Another high wind originally north of the vortex at $t = 86{,}400$ s moves to the west of the vortex. The northerly wind $hv_m = -546$ m^2 s^{-1} and $v_m = -5.74$ m s^{-1} ($v^*_m = -28.7$ m s^{-1}) west of vortex is stronger than southerly wind $hv_m = 526$ m^2 s^{-1} and $v_m = 5.58$ m s^{-1} ($v^*_m = 27.9$ m s^{-1}) northeast of the vortex. Consequently, the VC moves WSW with velocity $\mathbf{V}_{CV} = (-0.436, -0.076)$ m s^{-1}, ($\mathbf{V}^*_{CV} = (-2.18, -0.38)$ m s^{-1}). Stronger surface friction not only keeps the vortex further away from the Island but also enhances northerly flow. Consequently, the vortex moves southwestward without significantly northward rebound, as shown in D1, D6, and D9 in Fig. 5b and D2, D7, F2, and F3 in Fig. 5c, and Table 2b, c.

Group E: vortices with $a = 1 \times 10^{-5}\ m^{-1/2}\ s^{-1}$

This may be presented by E1 with $h_0' = 2$ m, $R = 16$ km, and $U = -1.6$ m s^{-1} ($R^* = 85$ km and $U^* = -8.0$ m s^{-1}) and initial at LC (280, 150) shown by magenta line with Δ in Fig. 5a. Figure 8a shows the streamlines, relative velocity V' (red), h' (purple dashed line), and PV (shaded color) at $t = 48{,}000$ s. The northerly maximum velocity, $v_m = -5.59$ m s^{-1} ($v^*_m = -28$ m s^{-1}), is slightly greater than the maximum southerly velocity $v_m = 5.50$ m s^{-1} ($v^*_m = 27.5$ m s^{-1}). Because of weak surface friction, the southward deflection and the slowdown of the vortex are small, and the vortex remains almost circular, although two excessive relative velocity maxima with $V' = 5.55$ m s^{-1} ($V^{*\prime} = 27.8$ m s^{-1}) show up on the front and rear of the vortex. The VC moves with velocity, $\mathbf{V}_{CV} = (-1.53, -0.05)$ m s^{-1} ($\mathbf{V}^*_{CV} = (-7.65, -0.25)$ m s^{-1}), from grid (186, 149) to grid (180, 148) between 48,000 and 51,200 s; it moves to (168, 147) at $t = 57{,}600$ s and to (158, 146) at $t = 64{,}000$ s (not shown).

After the VC landing, the northerly flow reaches the CMR and slows down, which becomes weaker than the southerly flow east of the vortex. The vortex slightly deflects north to (153,147) at $t = 67{,}200$ s (Fig. 8b). It moves to (142, 149) at $t = 73{,}600$ s (not shown) and continues moving west. Meanwhile, neither vortex deformation nor rotation of wind maxima is significant. Similar situation occurs to E_2 and E_3 in Fig. 5b and E_4, E_5, and E_6 in Fig. 5c. They are different from those with moderate to large surface friction, but close to the simulations over an idealized bell-shaped topography from the atmospheric models, i.e., the vortex gradually deflects south first, then rebounds north gently after landing, because the elevation along the eastern coast of the bell-shaped island is quite smooth and much lower than the mountains in the Eastern Taiwan. Hence, their track deflections are closer to our simulations with weak surface friction than moderate friction.

Group F: vorticities with $a = 1.5 \times 10^{-4}\ m^{-1/2}\ s^{-1}$

When F1 [with $h_0' = 2$ m, $R = 16$ km, $U = -1.6$ m s^{-1} ($R^* = 80$ km and $U^* = -8.0$ m s^{-1}), and initial at LN] approaching Taiwan, it gradually deflects south until $t \sim 48{,}000$ s, and then forms a loop between $t = 57{,}600$ and 76,800 s (Fig. 5a). The flow pattern of F_1 at $t = 57{,}600$ s (Fig. 9a) shows that the northerly velocity maximum, $v_m = -6.07$ m s^{-1} ($v^*_m = -30.4$ m s^{-1}), is greater than the southerly velocity maximum, $v_m = 5.18$ m s^{-1} ($v^*_m = -25.9$ m s^{-1}), east of the vortex. Hence, the vortex moves from (185, 166) to (181, 165) between $t = 57{,}600$ and $t = 60{,}800$ s (not shown). A weak secondary circulation is induced in the Taiwan Strait in Fig. 9a. The high-wind zones rotate and form a stronger westerly flow, $u_m = 6.5$ m s^{-1} ($u^*_m = 32.3$ m s^{-1}), south of vortex and a weaker easterly flow, $u_m = -5.98$ m s^{-1} ($u^*_m = 29.9$ m s^{-1}), north of vortex at $t = 67{,}200$ s when the VC is at (177, 161) (Fig. 9b). The VC moves eastward to (178, 160) at $t = 76{,}800$ s in Fig. 9c and the axis of vortex aligns NS direction. A narrow gap forms between the vortex and the Island; part of the easterly flow goes to the northern Taiwan with lower elevation and results in a weaker northerly channel flow, $hv_m = -476$ m^2 s^{-1} and $v_m = -4.93$ m s^{-1} ($v^*_m = -24.8$ m s^{-1}), and a stronger southerly flow, $hv_m = 590$ m^2 s^{-1} and $v_m = 6.18$ m s^{-1} ($v^*_m = 30.9$ m s^{-1}), east of the vortex. Hence, the vortex moves north and forms a loop. Then, it moves northwest around the northern tip of Taiwan, as shown in Fig. 5a, where a persistent strong wind shear exists between the ocean and the land, which is similar to loops observed in typhoon Krosa (2007) and typhoon Haitang (2005). They were discuss by Jian and Wu (2008) and Huang et al. (2011). Similar loops are also generated by vortex F_4 in Fig. 5b; and large vortices D_2, F_2, and F_3 in Fig. 5c.

As discussed in Fig. 1c, d, the basic flow has a tendency to deflect northward even without a vortex which may suggest that a vortex approaching northern Taiwan may

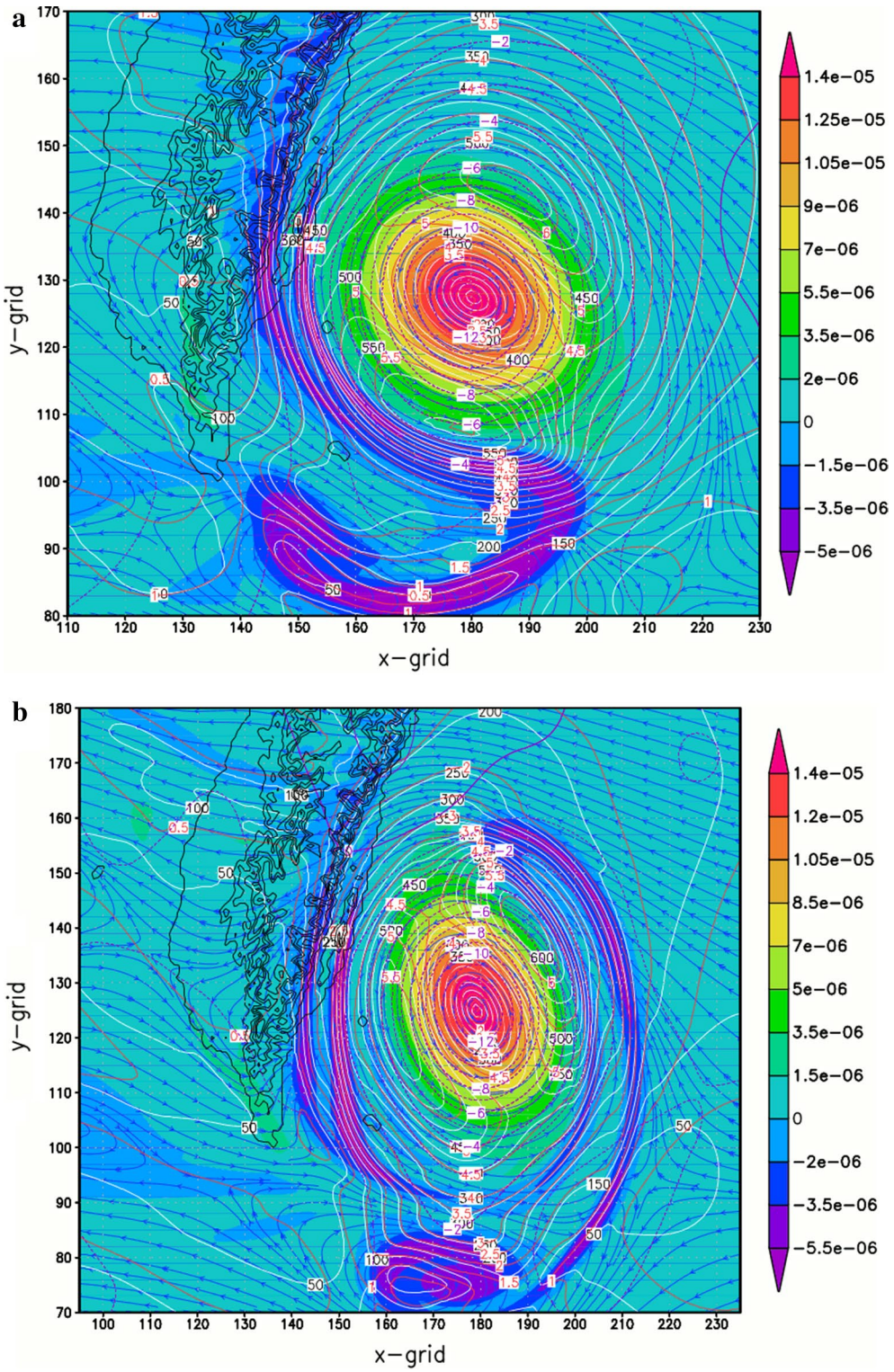

Fig. 7 Streamline, mass flux hV (*white*), surface depression *h′* (*dashed purple*), and *V′* (*red*) for D_1 at: **a** $t = 86{,}400$ s and **b** $t = 105{,}600$ s

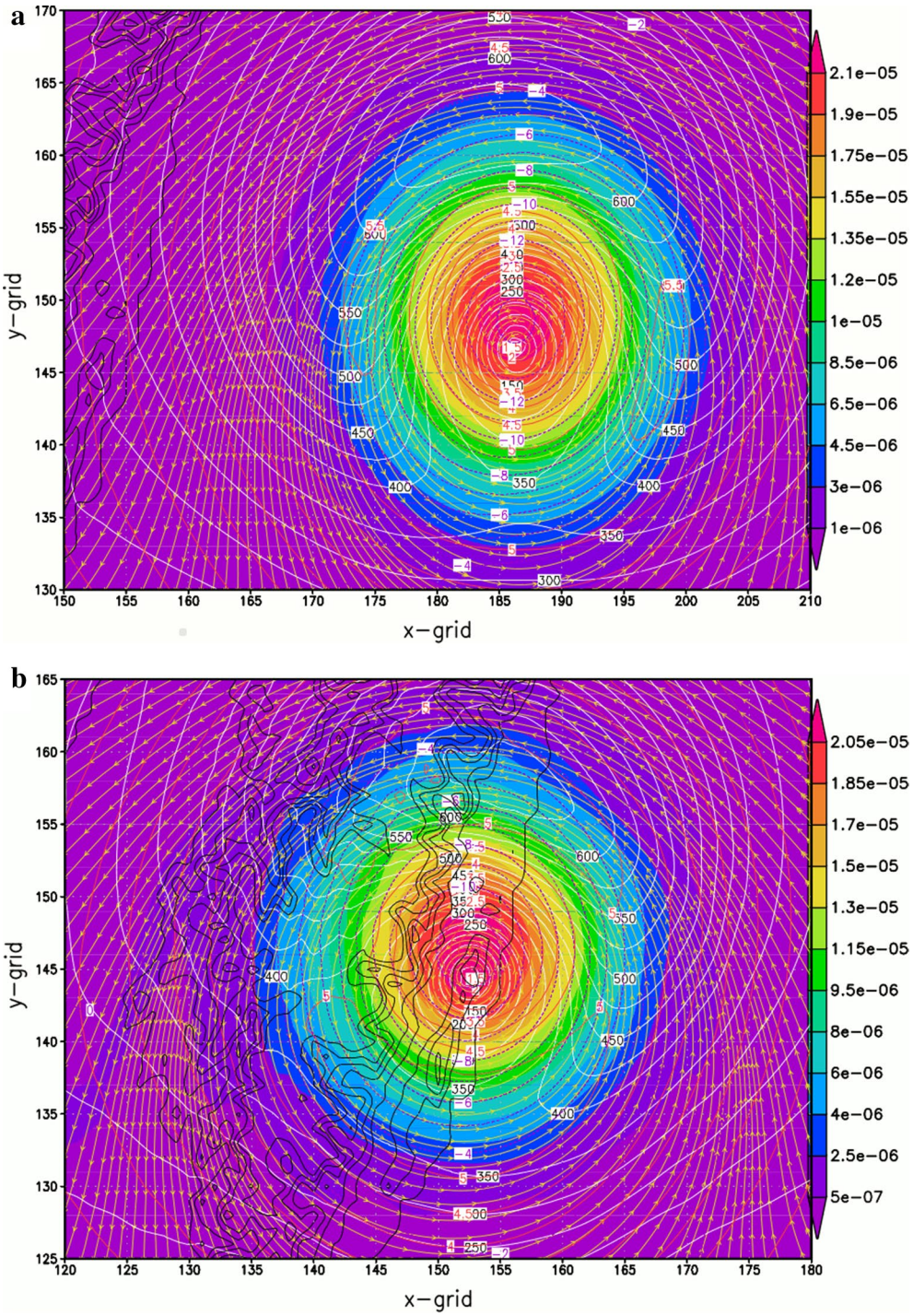

Fig. 8 Streamline, mass flux hV (white), surface depression h' (*dashed purple*), and V' (red) for E_1 at: **a** $t = 48{,}000$ s and **b** $t = 67{,}200$ s

turn northward easily. Besides, when a vortex approaching the northeast of the Island, part of circulation may reach the northern tip of Taiwan and beyond, which reduces the northerly channel flow; consequently, the vortex has tendency to deflect north.

A vortex comes from LC or LS, but it is still far away from the Island; the impinging angle between the coastal line and the outer flow is rather small, because Taiwan orients NNE–SSW instead of N–S. Hence, the outer flow is not much disturbed to force the vortex deflecting as in

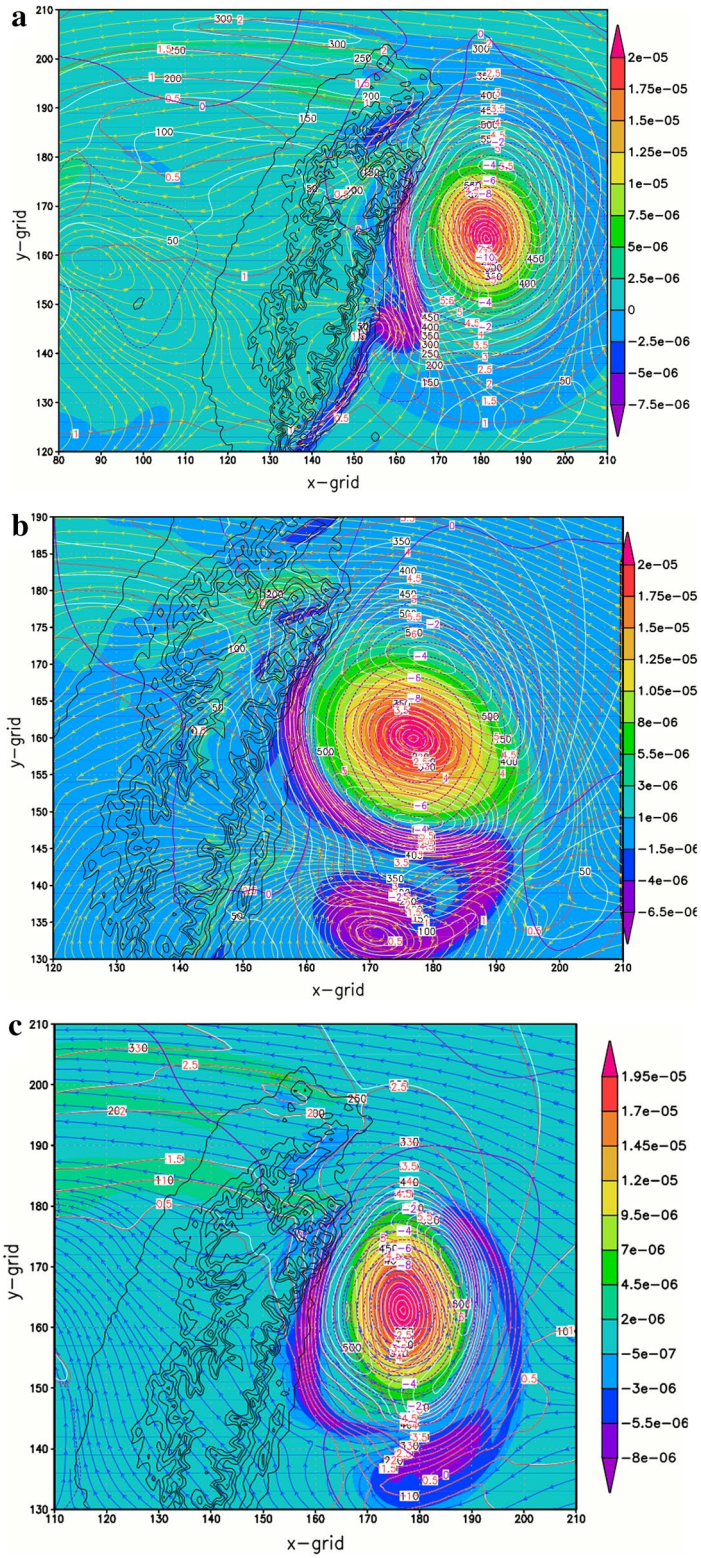

Fig. 9 Streamline, mass flux hV (*white*), surface depression *h′* (*dashed purple*), and *V* (*red*) for F_1 at: **a** $t = 57{,}600$ s, **b** $t = 67{,}200$ s, and **c** $t = 76{,}800$ s

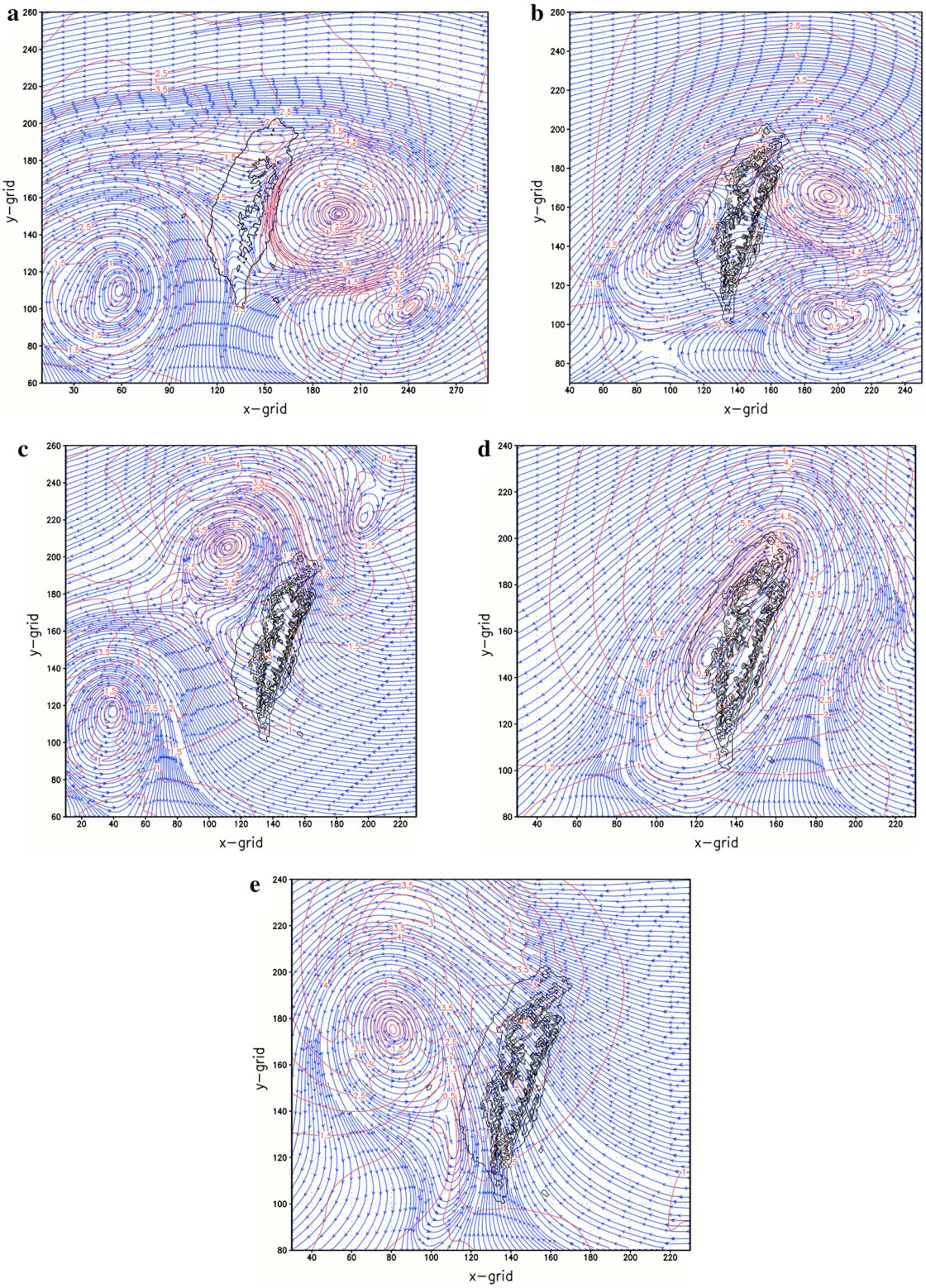

Fig. 10 Streamline (*blue*) and speed (*red*) for: **a** D_3 ($h_0' = 5$ m, $R = 40$ km, $U = -1.2$ ms^{-1}, $\alpha = 10^{-4}$ s^{-1} m$^{-1/2}$, LC) at $t = 124{,}800$ s, **b** D4 ($h_0' = 4$ m, $R = 40$ km, $U = -1.2$ m s^{-1}, $\alpha = 10^{-4}$ s^{-1} m$^{-1/2}$, LN) at $t = 76{,}800$ s, **c** D_4 at $t = 144{,}000$ s, **d** C_{10} ($h_0' = 4$ m, $R = 40$ km, $U = -1.2$ m s^{-1}, $\alpha = 3.5 \times 10^{-5}$ s^{-1} m$^{-1/2}$, LC) at $t = 96{,}000$ s, and **e** C_{10} at $t = 134{,}400$ s

some simulations with N–S bell-shaped island. After the vortex being closer to the Island, the channel effect shows up and the vortex starts to deflect southward due to the effect of channel flow and the formation of asymmetric inner circulation, which are consistent with an NNE–SSW island presented in Fig. 12a of Wu et al. (2015).

Induced secondary vortex

Induced vortices on the lee side have been simulated by the atmospheric models over an idealized bell-shaped island (Yeh and Elsberry 1993; Lin et al. 2005, etc.) When the vortex approaching Taiwan, flows may move around the Island or pass the CMR and induce secondary circulations. The flows of C_1 at $t = 124{,}800$ s (Fig. 6e) and F_1 at $t = 57{,}600$ s (Fig. 9a) show a weak, induced cyclonic circulation near southwestern coast of Taiwan.

A large, strong vortex D_3 (open red o in Fig. 5c) at $t = 76{,}800$ s can induce a large secondary circulation (Fig. 10a) on the lee side. As time increases, the secondary circulation propagates westward and becomes independent of the original vortex, which moves northwestward, then turns west passing the northern tip of Taiwan.

With large surface friction, vortex D_4 (red line in Fig. 5c) located to the northeast of Taiwan incites the secondary circulations on the west of the Island at $t = 76{,}800$ s (Fig. 10b). The original vortex continues to move around the northern coast. At $t = 144{,}000$ s, it moves to the NW of Taiwan, while the secondary circulation with significant velocity $V'_m \sim 3.5$ m s^{-1}, ($V'^*_m \sim 17.5$ m s^{-1}) propagates southwestward independently, as shown in Fig. 10c.

The case of C_{10} in Fig. 10d has the same parameters as D4 except a weaker surface friction (i.e., $\alpha = 3.5 \times 10^{-5}$ cyan line in Fig. 5c). A small secondary circulation is induced on the lee of the CMR over the land at $t = 96{,}000$ s when the original vortex move over the northern Island (Figs. 10d, 5c). The circulations of the original and induced vortices are tightly connected. At $t = 134{,}400$ s, the induced circulation is absorbed into the original vortex, as shown in Fig. 10e.

Conclusions

A shallow-water model was applied to study the deflection of a westbound vortex approaching Taiwan and the induced circulations on the lee side. The involved parameters are the mean flow, surface friction, size, intensity, and initial location of the vortex. The high-resolution, real topography simulations show that topography has little impact on the deflection in inviscid fluid, which was also proved by the PV-budget study. With small surface friction, when the vortex approaching Taiwan, it slightly deflects southward due to the enhancement of northerly channel flow, then rebounds northward when circulation reaching the CMR because of decrease of the channel flow by surface friction. This is consistent with the previous studies.

With moderate and large surface friction, when a vortex near Taiwan, surface friction creates a strong northerly channel flow west of the vortex. A strong southerly flow also forms east of the vortex, because the slowdown vortex is being pushed by the easterly flow from behind. Meanwhile, the vortex deforms. The asymmetric vortex and the accompanying two high-wind zones rotate cyclonically, while the vortex moves westward. At first, the northerly channel flow is stronger than the southerly flow east of the vortex, and the vortex deflects southward. The vortex deflects northward, when the stronger velocity shows up to the east of the vortex; it retreats east when the westerly velocity south of the vortex is stronger than the easterly flow north of the vortex. Therefore, the vortex not only can deflect south or north, but also can form a loop. The mechanism is different from the tradition theory of channel flow or the inner core asymmetric flow come from mid-troposphere (Wu et al. 2015). If cyclonic circulation of a large vortex moves around the northern coast, it can induce a strong secondary circulation on the west of the Island. On the other hand, the secondary circulation is rather weak when it is caused by the flow passing over the CMR.

Author details

[1] Department of Earth, Atmospheric, and Planetary Sciences, Purdue University, 550 Stadium Mall Drive, West Lafayette, IN 47907-2051, USA. [2] Hydrospheric Atmospheric Research Center (HyARC), Nagoya University, Furo-cho, Chikusa-ku, Nagoya 464-8601, Japan. [3] Department of Atmospheric Sciences, National Central University, Chung-Li, Tao-Yuan, Taiwan.

Acknowledgements

Part of this work has been done when the author was a visiting professor at Nagoya University and at National Central University. The author thanks Profs. Uyeda, Tsuboki, G. Lin, and M. C. Yen, C. Huang, P. Lin, and B. Jou for their helps and useful discussions, as well as Dr. W. L. Lee for providing Taiwan topographic data and Purdue University for providing the computing facilities. Reviewers' comments are also greatly appreciated.

Competing interests

The author declares no competing interests.

Received: 5 December 2015 Accepted: 9 June 2016
Published online: 08 July 2016

References

Bender MA, Tuleya RE, Kurihara Y (1987) A numerical study of the effect of an island terrain on tropical cyclones. Mon Weather Rev 115:130–155

Boyd JP (1980) Equatorial solitary waves. Part-1: Rossby solitons. J Phys Oceanogr 10:1699–1717

Boyd JP (1985) Equatorial solitary waves. Part 3: Westward-traveling motions. J Phys Oceanogr 15:46–54

Brand S, Blelloch JW (1974) Changes in the characteristics of typhoons crossing the island of Taiwan. Mon Weather Rev 102:708–713

Chang SW-J (1982) The orographic effects induced by an island mountain range on propagating tropical cyclones. Mon Weather Rev 110:1255–1270

Huang C-Y, Lin Y-L (2008) The influence of mesoscale mountains on vortex tracks: shallow-water modeling study. Meteorol Atmos Phys 101:1–20
Huang Y-H, Wu C-C, Wang Y (2011) The influence of island topography on typhoon track deflection. Mon Weather Rev 139:1708–1727
Jian G-J, Wu C-C (2008) A numerical study of the track deflection of Supertyphoon Haitang (2005) prior to its landfall in Taiwan. Mon Weather Rev 136:598–615
Lin Y-L, Chen S-Y, Hill CM, Huang C-Y (2005) Control parameters for tropical cyclones passing over mesoscale mountains. J Atmos Sci 62:1849–1866
MacCall BT, Wang Y, Sun WY (2015) A new semi-implicit time integration scheme for the time-dependent atmospheric boundary layer environment (ABLE) model. ARL-TR-7428. new ABLE) model. ARL-TR-7428
Matsuno T (1966) Quasi-geostrophic motions in the equator area. J Meteorol Soc Jpn 44:25–43
Peng M, Thompson WT (2003) Some aspects of effect of surface friction on flows over mountains. Q J R Meteorol Soc 129:2527–2557
Schar C, Smith RB (1993) Shallow-water flow past isolated topography. Part I: vorticity production and wake formation. J Atmos Sci 50:1373–1400
Shieh SS, Wang S-T, Cheng M-D, Yeh T-C (1998) Tropical cyclone tracks over Taiwan from 1897 to 1996 and their applications. CWB86-1 M-01, CWB, Taiwan, p 497
Sun WY (2007) Conserved semi-Lagrangian scheme applied to one-dimensional shallow water equations. Terr Atmos Ocean Sci 18(4):777–803
Sun WY (2010) Instability in leapfrog and forward–backward schemes. Mon Weather Rev 138:1497–1501
Sun WY (2011) Instability in leapfrog and forward–backward schemes: part II: numerical simulation of dam break. J. Comput Fluids 45:70–76
Sun WY (2013) Numerical study of severe downslope storm. Weather Clim Extrem. doi:10.1016/j.wace.2013.10.002
Sun WY, Chern JD (1993) Diurnal variation of lee-vortexes in Taiwan and surrounding area. J Atmos Sci 50:3404–3430
Sun WY, Chern JD (1994) Numerical experiments of vortices in the wake of idealized large mountains. J Atmos Sci 51:191–209
Sun WY, Chern J-D (2006) Numerical study of influence of mountain ranges on Mei-yu front. J Meteorol Soc Japan 84(1):27–46
Sun WY, Hsu WR (2005) Effect of surface friction on downslope wind and mountain waves. Terr Atmos Ocean Sci 16:393–418
Sun WY, Sun OMT (2013) Numerical simulation of Rossby wave in shallow water. Comput Fluids 76:116–127
Sun WY, Sun OMT (2015) 2015: Bernoulli equation and flow over a mountain. Geosci Lett 2:7. doi:10.1186/s40562-015-0024-1
Sun W-Y, Chern JD, Wu CC, Hsu W-R (1991) Numerical simulation of mesoscale circulation in Taiwan and surrounding area. Mon Weather Rev 119:2558–2573
Tang CK, Chan JCL (2013) Idealized simulations of the effect of Taiwan and Philippines topographies on tropical cyclone tracks. Q J R Meteorol Soc 140:1578–1589. doi:10.1002/qj.2240
Wang S-T (1980) Prediction of the movement and strength of typhoons in Taiwan and its vicinity. National Science Council Research Rep. 108, Taipei, p 100
Wu C-C, Li T-H, Huang Y-H (2015) Influence of mesoscale topography on tropical cyclone tracks: further examination of the channeling effect. J Atmos Sci 72:3032–3050
Yeh T-C, Elsberry RL (1993) Interaction of typhoons with the Taiwan topography. Part I: upstream track deflection. Mon Weather Rev 121:3193–3212